



HAL
open science

A two-scale approach to widen a predictive blast propagation model around a hemicylindrical obstacle

R. Gavart, S. Trélat, M.-O. Sturtzer, Nabiha Chaumeix

► To cite this version:

R. Gavart, S. Trélat, M.-O. Sturtzer, Nabiha Chaumeix. A two-scale approach to widen a predictive blast propagation model around a hemicylindrical obstacle. *Shock Waves*, 2023, 33 (3), pp.287-297. 10.1007/s00193-023-01135-4 . hal-04301993

HAL Id: hal-04301993

<https://hal.science/hal-04301993>

Submitted on 13 Dec 2023

HAL is a multi-disciplinary open access archive for the deposit and dissemination of scientific research documents, whether they are published or not. The documents may come from teaching and research institutions in France or abroad, or from public or private research centers.

L'archive ouverte pluridisciplinaire **HAL**, est destinée au dépôt et à la diffusion de documents scientifiques de niveau recherche, publiés ou non, émanant des établissements d'enseignement et de recherche français ou étrangers, des laboratoires publics ou privés.



Distributed under a Creative Commons Attribution 4.0 International License



A two-scale approach to widen a predictive blast propagation model around a hemicylindrical obstacle

R. Gavart¹ · S. Trélat¹ · M.-O. Sturtzer² · N. Chaumeix³

Received: 23 September 2022 / Revised: 27 April 2023 / Accepted: 27 April 2023 / Published online: 16 June 2023
© The Author(s) 2023

Abstract

The aim of the present paper was to report on an experimental study of the characterization of a blast wave initiated by a solid explosive and its interaction with a rigid obstacle in the form of a hemicylinder. Pressure transducers located along the path of the blast wave and high-speed imaging allow (1) the measurement of the overpressure at different locations and (2) the characterization of the blast wave inception, propagation, and reflection off the hemicylinder. The scaling effect has been investigated by performing experiments in two different facilities, where one is at twice the scale of the other.

Keywords Blast wave · Hemicylindrical obstacle · Multi-scale · Phenomenological model · Condensed explosive

1 Introduction

Nowadays, the protection of infrastructure and personnel against damage caused by explosions is a very important field of research and development. These explosions generate blast waves that need to be characterized in order to evaluate their effects. The ability to predict the effect of a blast wave on a given structure is not straightforward and relies on experimental investigations [1] and numerical modeling [1–3]. The experimental studies are usually conducted in small-scale facilities which allow better monitoring by combining different diagnostic methods [4, 5] and providing the ability to better control and to vary the conditions for blast wave generation and the interaction with various geometrical configurations. So far, numerous studies have focused on blast wave propagation in air and established correlations predicting incident overpressures in the free field [6–8]. The

American United Facilities Criteria (UFC) [9]—a military construction guide—also developed abacuses to predict various blast wave parameters depending on the scaled distance. The use of these correlations, paired with similitude principles, such as in [10], allows the determination of blast wave parameters at different scales.

Regarding the interaction with structures, several studies focused on the mitigating properties of barriers [11, 12]. Sochet et al. [13] studied the influence of a trapezoidal protective barrier on blast propagation. Their setup featured a gaseous explosive charge composed of stoichiometric oxygen and propane, ignited by an exploding wire. Two types of barriers, designed according to NATO recommendations, were tested: type A barriers with 45° inclined walls both upstream and downstream and type B with 45° and 90° inclined walls upstream and downstream (and vice versa). These were placed from 0.07 to 0.1 m away from the charge. The study showed that barriers with vertical walls were more efficient in attenuating overpressure downstream and prevented the rapid formation of a Mach stem. However, vertical walls produce higher overpressure levels on the upstream face. Nevertheless, a type B barrier with the vertical wall on the downstream face produces the same attenuation and can thus be used to have lesser reflected overpressures on the front face.

Gautier et al. [14] studied the interaction of a blast wave with a planar wall measuring the influence of its length on the shock propagation and maximum overpressure downstream. Twelve different wall lengths were exposed to the blast wave

Communicated by G. Ciccarelli.

This paper is based on work that was presented at the 28th International Colloquium on the Dynamics of Explosions and Reactive Systems (ICDERS), Naples, Italy, June 19–24, 2022.

✉ R. Gavart
raphael.gavart@cnrs-orleans.fr

¹ IRSN - French Institute for Radioprotection and Nuclear Safety, Fontenay-Aux-Roses, France

² ISL - French-German Research Institute, Saint-Louis, France

³ CNRS-ICARE, Orléans, France

generated by the detonation of a gaseous explosive charge on a detonation table. Several pressure sensors were placed on the table, downstream from the wall, and a high-speed camera captured the blast wave propagation around the obstacle via pure in-line shadowscopy. These experiments showed that the wall reduces the maximum overpressure downstream close to the wall. However, if the wall is not at least three times longer than the height, circumventing waves (i.e., diffracting around the lateral sides of the wall) could catch up with the wave propagating over the wall, and the protective effect could be negated.

Other authors have focused on the evolution of overpressure and reflection at the surface of obstacles [15, 16]. Geva et al. [17] studied the regular reflection–Mach reflection transition criterion in unsteady flows at the surface of cylindrical convex obstacles. Tests were performed in a shock tube with shock Mach numbers of 1.3 and 1.5. Based on high-speed imaging, the transition over a convex obstacle has been identified as occurring when both incident and reflected shock waves become perpendicular.

The propagation of a blast wave around an arch (half-cylinder) obstacle and the overpressure it generates were studied by Glasstone [18]. Based on nuclear explosion results, he proposed a model describing the evolution of overpressure, rise time, and drag coefficient over the arch surface. This model applies for structures subjected to overpressures below 3.45 bar (50 psi) and located in the Mach reflection region.

Finally, a model predicting the blast wave overpressure on the back face of a hemicylindrical obstacle was proposed by Trélat et al. [5]. This work featured small plastic explosive charges (50 g TNT equivalent) and a rigid hemicylinder placed at various distances from the charge on a blast table. This hemicylinder was equipped with piezoelectric and piezoresistive pressure sensors. The recorded overpressure was used to fit a second-order polynomial equation describing the evolution of overpressure on the back face of the hemicylinder. In this study, we extend the model to double scale and capture additional data at different reduced distances.

We provide an experimental study on the blast wave characterization initiated by a solid explosive detonation and their interaction with a non-deformable hemicylindrical obstacle. The coupling between pressure measurements along the path of the blast wave and high-speed background-oriented schlieren (BOS) imaging allows (1) the measurement of the overpressure at different locations and (2) the characterization of the blast wave generation, propagation, and reflection off the hemicylinder. The scaling effect has been investigated by performing reduced-scale experiments at two different facilities: (1) Institute for Radioprotection and Nuclear Safety (IRSN) and (2) French-German Research Institute of Saint-Louis, France (ISL).

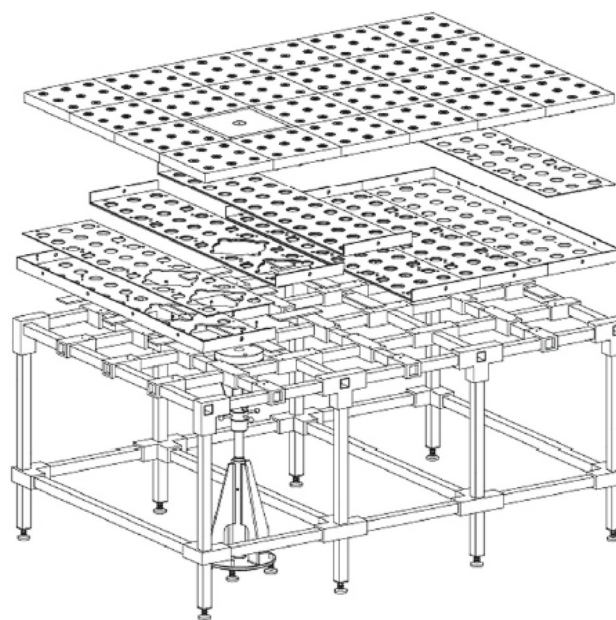


Fig. 1 The modular table, from [7]

2 Experimental setups

2.1 IRSN experimental setup

The IRSN-blast table is currently hosted at the ArianeGroup in Vert-le-Petit (Centre de Recherche du Bouchet). It has enabled IRSN to carry out different experimental campaigns over the last 15 years, the results of which have been published in [5, 7].

The indoor experimental setup includes a 2.40 m × 1.60 m blast table [7] that supports a four-section rigid, non-deformable wooden hemicylinder (400 mm diameter and 1.60 m length) and an explosive charge. This hemicylinder was designed to be considered as non-deformable. The table, shown in Fig. 1, is composed of modular square wooden plates (400 mm × 400 mm × 50 mm), each drilled with nine holes to flush mount pressure sensors (each separated by 133 mm), or if not used a metallic plug. A special module designed to withstand the explosion pressure is made of steel (Fig. 2); the charge stand is inserted in this module and is drilled to allow the detonator to reach the base of the charge. All these parts make the table highly modular, allowing the flexible positioning of the explosive charge and the pressure sensors on the entire table surface. This also allows the adjustment of the hemicylinder to charge distance ranging from 0.27 to 1.60 m. The table was designed so as to minimize vibrations and shock wave transmission between the modules to improve the repeatability of tests.

The hemicylindrical obstacle is composed of a wooden external layer (Fig. 3) and consists of four 400-mm-long and 400-mm-diameter sections. The 1.60-m-long hemicylinder is

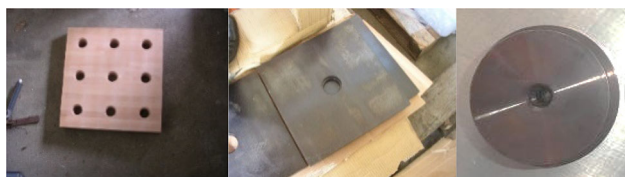


Fig. 2 Wooden modular plate (left), steel plate (middle), and charge and detonator support (right), which are part of the IRSN detonation table



Fig. 3 IRSN experimental setup with a 41.5-g Hexomax® charge—27 cm between the charge and hemicylinder

as wide as the table, limiting the circumventing of the blast wave. Only one section of the obstacle is instrumented that includes 15 sensor positions distributed in three rows: a central row and two parallel ones located at 100 mm away on both sides. This instrumented section is reinforced by an internal steel structure. Each row can host five sensors distributed every 30° (e.g., one sensor at 30°/60°/90°/120°/150°).

The blast wave generated by the detonation of the explosive charge produces a blast wave for which the pressure–time history is measured with piezoelectric and

piezoresistive sensors. The piezoelectric sensors are Kistler 603B and 603CA (connected to Kistler 5011 and 5018 charge amplifiers), and the piezoresistive ones are Kulite XTL-190 (Vishay 2311 charge amplifiers). They are labeled P_i ($i \in \{1, 3, 4, 5\}$) for Kulite sensors and K_j ($j \in \{1, \dots, 11\}$) for Kistler ones. Table 1 presents the position of these sensors for the tests performed in free field or with the presence of the hemicylinder. For tests involving the hemicylinder, sensors K3, K4, K6, K7, and K8 were placed on the central line of the hemicylinder, and sensors P1, P3, P4, and P5 were placed on a parallel line, respectively, at 30°, 90°, 120°, and 150°. Sensor P1 was placed at 150° for tests with hemicylinder at 27 cm from the charge (as shown in Fig. 4) because it could not withstand the peak pressure encountered on the front face in close range.

Sensors K10 and K11 were in the same position for all the tests; these reference sensors allowed to verify the reproducibility of measurements and their agreement with reference theoretical values such as in [6, 19].

The results are acquired by a 500-kHz Nicolet Genesis acquisition system (Bridge 1M iso Card, 24 channels) and filtered at 125 kHz (FIR filter, -0.1 dB cut-off frequency).

2.2 ISL experimental setup

Experiments at ISL were conducted on a blast measurement pad located at the experimental test range in Baldersheim. This concrete blast pad is twice the scale of the IRSN-blast table and also allows to perform tests in free field or with obstacles. It is composed of a concrete pad equipped with a steel block filled with absorbent material that cushions pressure waves generated by explosive charges detonated on the ground.

Table 1 Sensors positioning on the detonation table during tests

Distance to the charge (m)/scaled ($\text{mkg}^{-1/3}$)	Test configuration—distance charge–hemicylinder			
	Free field	27 cm	100 cm	160 cm
0.27/0.57	K1 K10 P1	K10	K10	K1 K10
0.30/0.64	P3 P4 P5	HC		
0.80/1.72		K5		
0.93/2.01	K2 K11	K2 K11	K2 K11	K2 K11
1.07/2.30	K3	K9	HC	
1.20/2.58		K1		
1.33/2.87	K4			
1.47/3.16	K5		K5	K5
1.60/3.45	K6		K1	HC
1.73/3.73	K7		K9	
2.00/4.31	K8			
2.13/4.60				K9
2.21/4.75	K9			
HC hemicylinder				

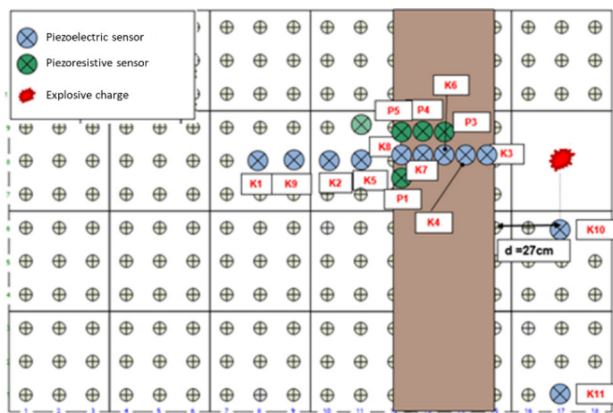


Fig. 4 IRSN-blast table configuration for tests with the hemicylinder 27 cm away from the charge

A metallic rail was inserted from the charge support plate to the edge of the pad providing 22 possible sensor positions, each separated by 266 mm, twice the distance between sensors used in the IRSN experiments.

A steel non-deformable hemicylindrical obstacle twice the size of the one used in the IRSN experiment was placed in front of the explosive charge, normal to the pressure measurement rail axis (Fig. 5). The hemicylinder is made of four 800-mm-long sections, with a diameter of 800 mm, for a total length of 3.2 m. Pressure sensors can be placed every 30° in three rows of holes drilled in the hemicylinder: a central one and two lateral rows positioned 50 mm on each side. Sensors are mounted on the obstacle with polypropylene intermediate inserts. The target hemicylinder can be placed at different distances to the charges ranging from 53 cm to 3.2 m.

The central line of sensors is equipped with five PCB 113B28 piezoelectric pressure gauges connected to 482A22 signal conditioners, while the second one is equipped with five Kulite XT190 piezoresistive pressure sensors connected to a Kyowa CDV 700A conditioner. An additional PCB pressure sensor (labeled PArr) was placed in the metallic rail in the first available position behind the hemicylinder (26.6 cm behind for 53-cm and 3.2-m configuration and 13.3 cm for 2-m configuration, Table 2). A pencil pressure probe (labeled PPencil) was also installed on a mobile pole opposite to the obstacle to measure pressure evolution in free field, at the same distance from the charge as sensor PArr; it is visible on the left side of Fig. 5. Their position for each test is listed in Table 2.

Sensors on the hemicylinder are labeled “P XY,” where X represents the row index and Y the position of the sensor: Sensor P31 is the sensor located at position 1 (30°) on the median row, whereas sensor 25 is located at position 5 (150°) on the next row, as depicted in Fig. 6.

Data are recorded and filtered (fifth-order Bessel filter, 500 kHz) by a 2-MHz Transcom Recorder.



Fig. 5 ISL experimental setup with a 333-g Hexomax® charge—53 cm between the charge and hemicylinder

All ISL-blast waves are also recorded with a V310/V311 pair of Phantom cameras (Fig. 7), using a 135-mm F/2 Nikon lens, at a frame rate of 10,000 frames per second (fps) and a 400×600 px².

2.3 Explosive charges

Hexomax® plastic explosive (produced by Eurenco) was used to form the hemispherical charges. The TNT equivalency of Hexomax® provided by ArianeGroup is 1.2, defined as the ratio of the energy per unit mass released by Hexomax® and TNT during the expansion of their detonation products.

At IRSN, the Hexomax® charges are formed manually in a metallic mold and ignited by a Davey–Bickford SA4201A detonator containing 140 mg of lead azide (primary explosive) and 100 mg of PETN. The detonator is inserted in the central hole of the charge support shown in Fig. 2. To achieve a TNT equivalent mass of 50 g, each charge weighed 41.5 g. Each test is repeated three times to analyze reproducibility and repeatability of the explosive charges and to allow a statistical analysis of data recorded.

The explosive charges used at ISL are twice the diameter of those used at IRSN and eight times its mass, i.e., 333 g of Hexomax® equivalent to 400 g of TNT. Each test was repeated four times; this allowed to extend the studied field of view around the hemicylinder with no image resolution loss. Charges were ignited with a RP83 exploding bridgewire detonator from Teledyne Defense, which contains 86 mg of PETN, 123 mg of RDX booster, and finally 908 mg of HMX [20].

Table 3 summarizes experimental conditions used at both facilities according to the similitude principle, and Appendix presents trials' denomination.

Table 2 Sensors positioning on the blast pad during tests

Distance to the charge (m)	Scaled distance to the charge ($\text{m kg}^{-1/3}$)	Charge to hemicylinder distance		
		53 cm	200 cm	320 cm
0.53	0.57	HC		
1.60	1.72	PArr PPencil		
2.00	2.15		HC	
2.93	3.16		PArr PPencil	
3.20	3.45			HC
4.27	4.60			PArr PPencil

HC hemicylinder

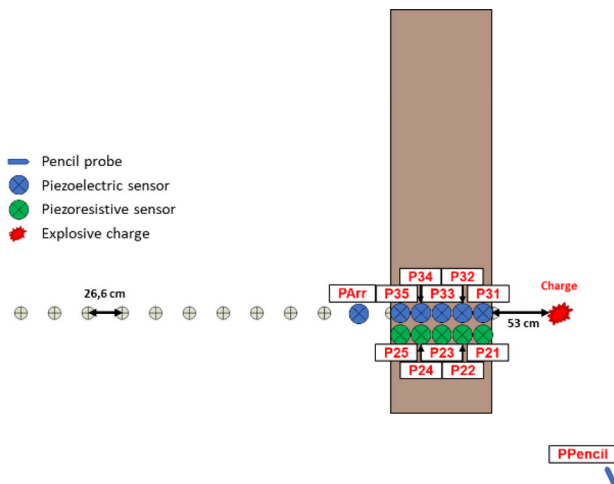


Fig. 6 ISL-blast pad configuration for tests with the hemicylinder 53 cm away from the charge

3 Results

Three main parameters describing the positive phase of a blast wave were studied:

- Time of arrival t_a (s);
- Peak maximum overpressure ΔP_{max} (bar);
- Positive impulse I^+ (bar s).

The positive impulse is defined as the area under the positive part of the pressure–time profile:



Fig. 7 High-speed camera used during ISL tests (V310 Phantom camera)

$$I^+ = \int_{t_a}^{t^+} P(t) dt, \tag{1}$$

where t_a is the time of arrival of the blast wave, t^+ is the end time of its positive phase, and $P(t)$ expresses overpressure as a function of time.

Table 3 Similitude principle applied to the two-scale study

	IRSN scale	ISL scale
Hemicylinder diameter (m)	0.40	0.80
Hemicylinder length (m)	1.60	3.20
Sensors spacing (m)	0.13	0.27
Charge/hemicylinder distances (m)	0.27–1.60	0.53–3.20
Reference explosive charge (g TNT eq.)	50	400

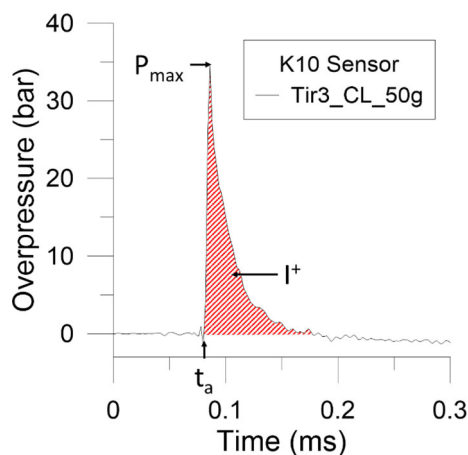


Fig. 8 Example of a pressure signal obtained during IRSN free-field tests

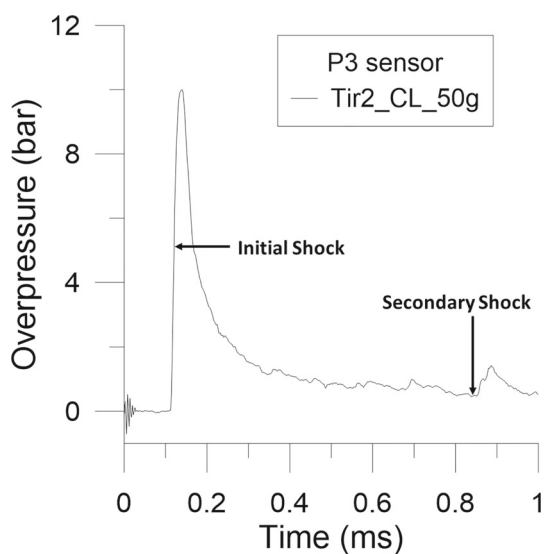


Fig. 9 Example of a piezoresistive pressure signal without a negative phase— $0.64 \text{ m kg}^{-1/3}$

A temporal pressure profile recorded during free-field tests at IRSN is shown in Fig. 8; the piezoelectric sensor was located 27 cm from the explosive charge (50g TNT equivalent).

Positive impulses of pressure signals were computed using Grapher 11. However, it was not possible to calculate the one from piezoresistive sensors as they did not display any negative phase ending the positive phase. One of these signals is presented in Fig. 9. The absence of a negative phase may be due to the arrival of the secondary shock, visible around 0.85 ms, or sensor signal drift due to thermal effects from the fireball.

The scatter in a set of experimental values is defined as the standard deviation of the set divided by its mean value.

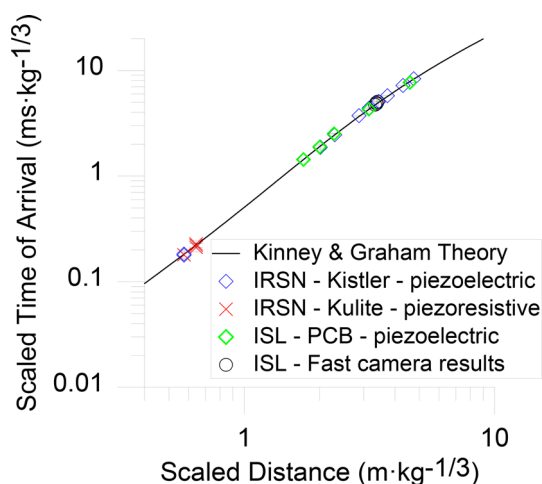


Fig. 10 Times of arrival measured at IRSN and ISL versus Kinney and Graham’s theory

3.1 Free-field pressure measurements

In Figs. 10, 11, and 12, IRSN piezoelectric sensors are represented as blue crosses, piezoresistive ones as red crosses, and ISL piezoelectric sensor results as green diamonds.

Times of arrival obtained with the two types of sensors are in good agreement with the theoretical values from [6], as shown in Fig. 10. Data obtained from the high-speed video are also in very good agreement with Kinney and Graham’s predictions [6] and sensor results. Symbols represent experimental data, each point being the mean value of a series of tests and error bars representing the standard deviation of these series, which is defined as:

$$\sigma = \sqrt{E[(X - E(X))^2]}, \tag{2}$$

where X represents a series of experimental values. The solid line represents the prediction from Kinney and Graham [6]. This difference in the IRSN and ISL data is < 5%.

Figure 11 presents a comparison of the normalized overpressure obtained using both sensor technologies with the overpressure predicted by Kinney and Graham [6] provided in (2). It also shows experimental data obtained by Sturtzer et al. [21] using piezoresistive sensors; these data were obtained in the same facilities as the present study, using the same Hexomax® charges.

At close range, the measured overpressures from the piezoresistive sensors are lower than those from the piezoelectric ones by 55% at 27 cm from the charge center. Values recorded by piezoelectric sensors are close to Kinney and Graham’s predictive equation [6]:

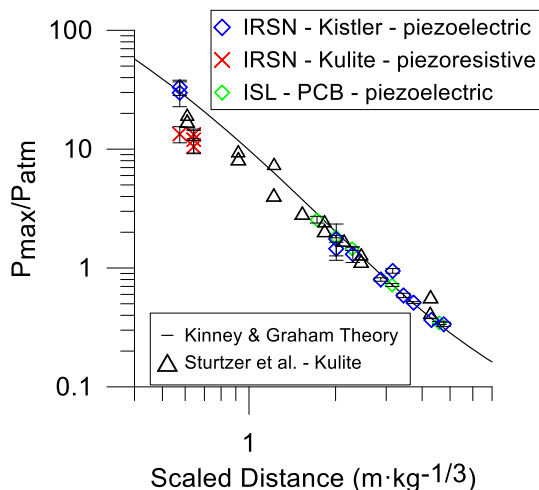


Fig. 11 Peak overpressures measured at IRSN and ISL versus Kinney and Graham’s theory

$$\frac{P_{max}}{P_{atm}} = \frac{808 \left(1 + \left(\frac{z}{4.5}\right)^2\right)}{\sqrt{1 + \left(\frac{z}{0.048}\right)^2} \sqrt{1 + \left(\frac{z}{0.32}\right)^2} \sqrt{1 + \left(\frac{z}{1.35}\right)^2}}, \quad (3)$$

where z ($m \cdot kg^{-1/3}$) is the scaled distance to the explosive charge, P_{max} (bar) the peak overpressure, and P_{atm} (bar) the ambient pressure.

It is clear that in Fig. 11, the overpressure data measured by piezoelectric sensors follow the trend predicted by [6] at both scales, even though the scatter in the experimental data for the close range sensors is high. These data are also consistent with overpressure data obtained by Sturtzer et al. [21].

Regarding the positive impulse, the results from piezoelectric sensors follow the trend predicted by [6], but with a rather large difference. At close range, measurements are 46% higher than predicted values with a large scatter in the data. The data for longer range lie below the Kinney and Graham predictions (down to -26%), but are more repeatable, as shown in Fig. 12, with $< 10\%$ scatter.

The slight difference between ISL and IRSN measured positive impulse may be attributed to the fact that the detonation wave propagates differently in the two charges as the mass ratio between the detonator and the explosive charge is different. It could also be due to the presence of the damping material in both charge supporting systems, potentially inducing energy losses. Finally, impulses were determined using an above-ground pressure sensor at ISL, whereas the IRSN sensors were mounted on the surface of the blast table. It would be interesting to collect more data to fill the gap in the data between 0.6 and $2 m \cdot kg^{-1/3}$ in Fig. 12.

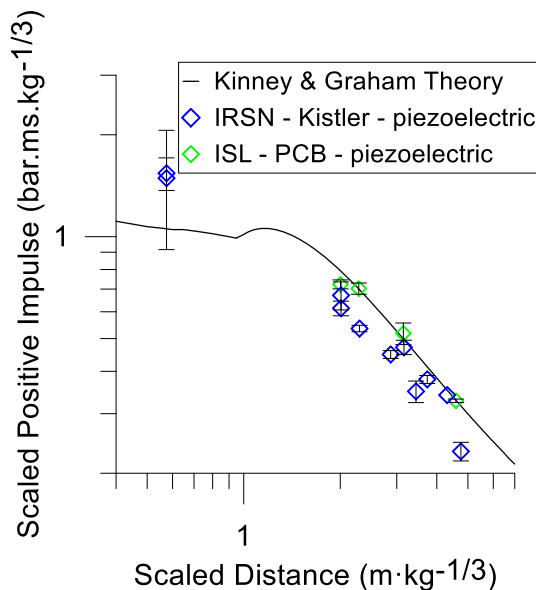


Fig. 12 Positive impulses measured at IRSN and ISL versus Kinney and Graham’s theory

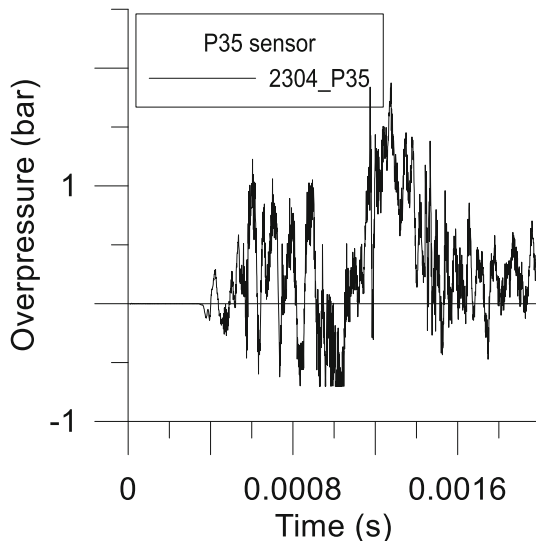


Fig. 13 Example of a perturbed signal from a piezoelectric sensor for the 53-cm configuration at ISL

3.2 Hemicylinder pressure measurements

This section will present the results obtained with the sensors placed on the surface of the hemicylinder at both scales. Unfortunately, due to the experimental setup at ISL, the impact of the blast wave on the structure induced significant vibrations. In close range, this made P35 signals (150°) unusable as the generated noise amplitude exceeded the signal amplitude, as depicted in Fig. 13.

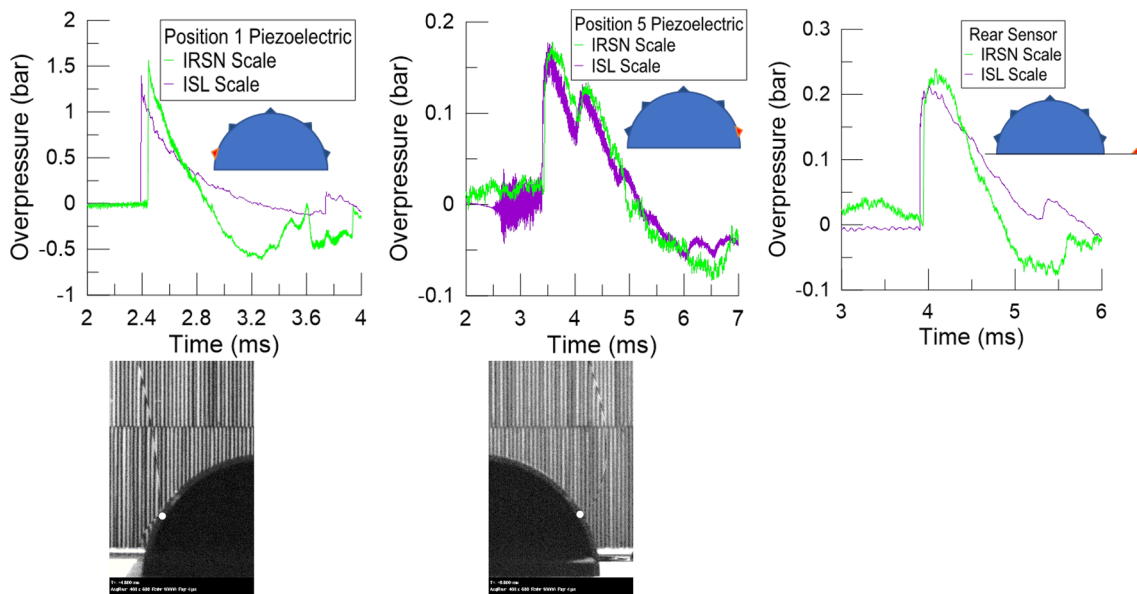


Fig. 14 Comparison of piezoelectric pressure signals obtained at both scales: 1.6 m (green line)/3.2 m (purple line)—camera images illustrate the shock structure as it hits sensors positions (white dots)

Signals recorded at position 5 at both scales are extremely similar, as shown in Fig. 14 (middle), where the pressure signals are overlaid on each other. However, different profiles shapes were observed at some sensor positions. Figure 14 (left) presents a comparison of signals recorded by piezoelectric sensors at position 1 (at 30°) at both scales; it appears that IRSN pressure signal shows a more significant pressure decay after the pressure peak and a lower minimum pressure. This effect seems to be due to sensor drift, as this is the only sensor presenting such a behavior. This kind of behavior was also observed by Grosseuvres et al. [22].

A difference is also observed between pressure profiles recorded by the sensor placed on the floor behind the hemicylinder, as shown in Fig. 12 (right). The signal obtained at IRSN scale presents a larger overpressure decay. Nevertheless, for the configuration with the hemicylinder placed 1.6 m away from the explosive charge, this sensor position ends up at only 7 cm from the edge of the table. Therefore, when the blast wave reaches this location, the diffraction at the end of the table may amplify the decay of the blast.

These differences in pressure profiles, measured blast time of arrival, and peak overpressure are analyzed in the following section. As illustrated in Fig. 15, the blast wave time of arrival recorded at both scales presents a very good scattering, globally < 6%. The largest scatter is observed at close range, on the front face of the obstacle, where the scatter for the 30° sensor at ISL reaches 11%. To compare results, the blast wave time of arrival recorded at ISL was divided by two; the relative difference between the two scales is < 4%.

The same is true for measured peak overpressures, represented in Fig. 16. The largest scatter is observed in the close

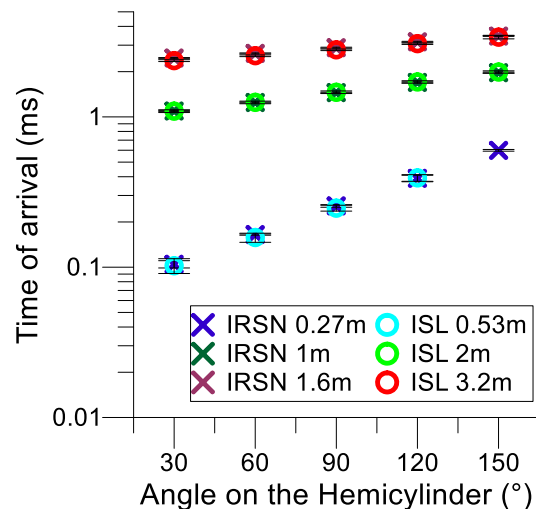


Fig. 15 Comparison of times of arrival measured at ISL and IRSN at the hemicylinder surface

range data, where the effect of the fireball is most important, with a peak at 28% for the 30° sensor of ISL, whereas the overall scatter is < 15% at both scales. Likewise, the highest difference between the two scales is observed in close range, up to 25%, whereas it is below 10% at further distances.

Thereby, it seems that the similitude principle from [10] is still applicable for peak overpressures and blast wave time of arrival in the presence of an obstacle in the studied range of reduced distance (0.57 to $3.45 \text{ m kg}^{-1/3}$).

This study also allowed to witness a difference of behavior between the two sensors technologies, namely piezoelectric and piezoresistive. As aforementioned, a discrepancy in the

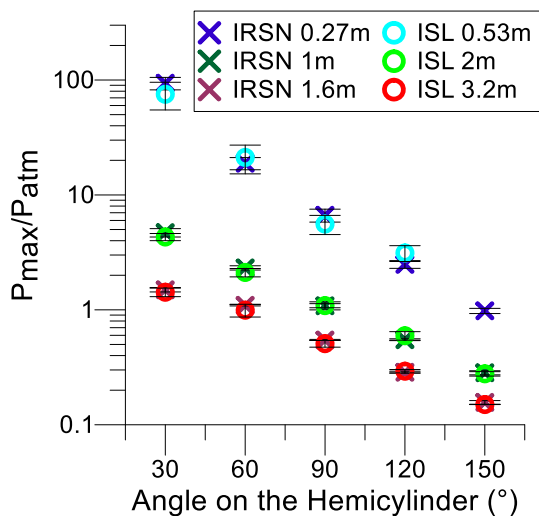


Fig. 16 Comparison of peak overpressures measured at ISL and IRSN

measurement of peak overpressure in the free field, piezoresistive sensor recording is far inferior in close range. The comparative use of the two technologies side by side at the surface of the hemicylinder also demonstrated this difference, as observed in Fig. 17.

Piezoresistive sensors demonstrate longer response times, as the rising edge is less steep than for piezoelectric sensors. Thus, they may present a larger difference in the real peak overpressure because of their slow response time. The difference between technologies lessens when the hemicylinder is placed further from the charge, or when considering a sensor position further along the arc of the obstacle. For example, there is no difference in the signals recorded by both technologies at 150° with the obstacle at 3.2m from the charge, as displayed in Fig. 18. Technical data provided by sensors manufacturers are not sufficient to interpret these response differences. They may be explained by the slower rise time phenomena taking place in these configurations, which would allow piezoresistive sensors to “catch up” with piezoelectric ones. Moreover, they seem to be less affected by vibrations than their piezoelectric counterparts.

4 Analysis

Overpressure results obtained at the surface of the obstacle have been compared to the model described in [5] (referred to as Model S). The use of a transmission coefficient C_t , defined as the measured overpressure at a given position divided by the free-field overpressure at the same position, allows the study to compare results obtained at both scales directly. The model proposes to calculate this transmission coefficient as a function of a reduced shifted direct distance (RSDD), defined in Fig. 19, based on the geometry of the obstacle:

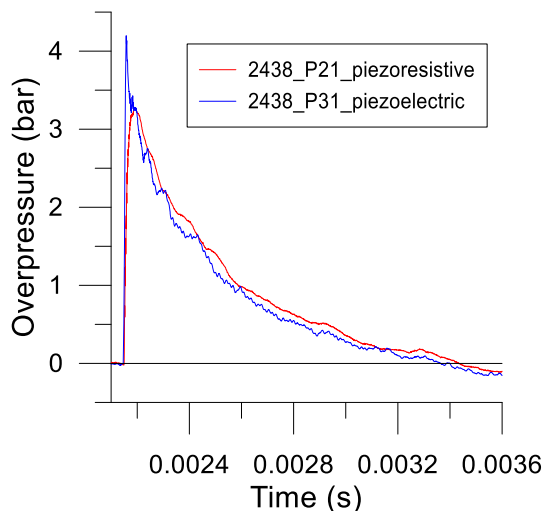


Fig. 17 Comparison of overpressure signals obtained with piezoelectric and piezoresistive sensors at 30° at ISL—2-m configuration

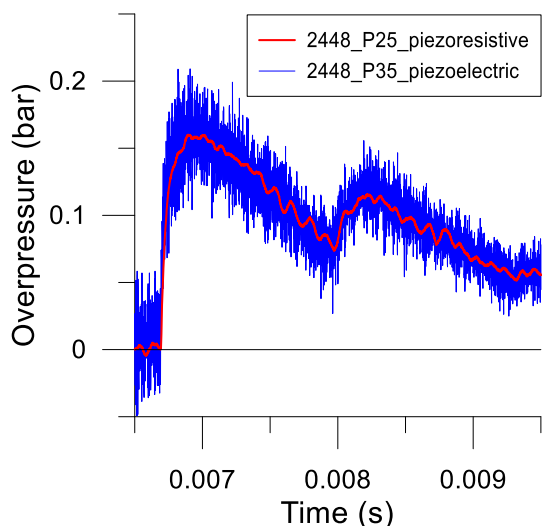


Fig. 18 Comparison of overpressure signals obtained with piezoelectric and piezoresistive sensors at 150° at ISL—3.2-m configuration

$$C_t = 0.396 \times RSDD^2 - 1.4385 \times RSDD + 1.347. \quad (4)$$

This model is valid for positive RSDD and was designed with results obtained at three charge-to-obstacle distances at IRSN reduced scale (0.4, 0.6, and 1.6 m) with piezoelectric sensors. Thus, only the results from piezoelectric sensors are compared here.

The latest experimental campaigns allowed to record data at new distances at IRSN reduced scale (0.27 m and 1 m) to validate the model and additional data at 1.6 m (120° results were missing in the model) from the charge. Experiments carried out at ISL also allow to compare large-scale results to the model, in addition to studying scale effects. The comparison of the new results with Model S is presented in Fig. 20. It appears that the IRSN results are very close to the model

Fig. 19 Definition of the reduced shifted direct distance, from [5]

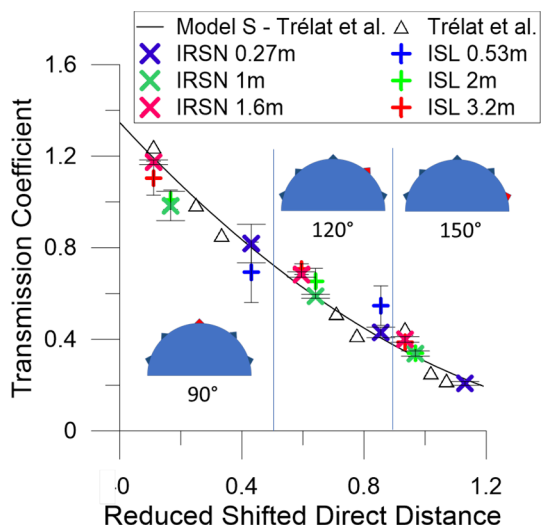
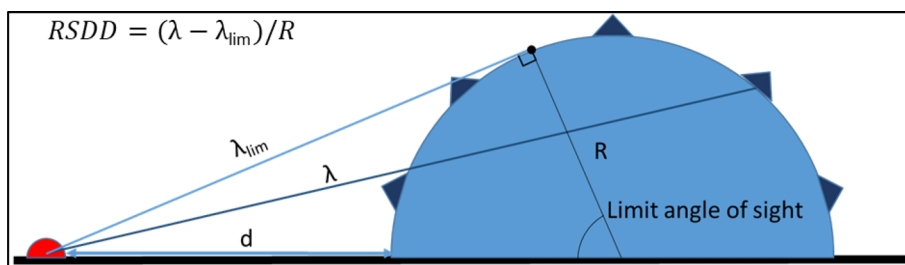


Fig. 20 Comparison between experimental results from both scales with Model S from [5]

at 120° and 150°. The ISL results seem to be less close to the model, but the data also present larger scatter, especially in close range, so they could be closer to the model. Overall, the results appear to follow the trend predicted by the model.

Model S seems to slightly overestimate overpressures at 90°, where results are 7% inferior to the model in average, as depicted in Fig. 21. However, on the back face of the hemicylinder the experimental data are above the model with 12% difference in average at 120° and 5% at 150°.

5 Conclusion

The two setups developed at IRSN and ISL allowed to study blast wave interaction with a hemicylindrical structure at different scales. The present study provides new peak overpressure data obtained at two scales. The results highlighted the difference of behavior between piezoelectric and piezoresistive sensors, the latter being much slower, leading to an underestimation of peak overpressure measured on the front

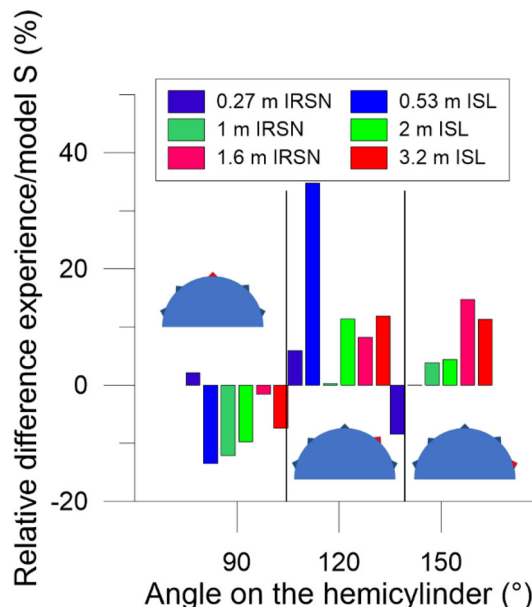


Fig. 21 Difference between experimental transmission coefficients and Model S at both scales

face of the hemicylinder and for reduced distances less than $0.64 \text{ m kg}^{-1/3}$. These data also confirmed the applicability of the similitude principle even in the presence of an obstacle for blast parameters such as peak overpressure and blast wave time of arrival. Finally, new experimental results were compared to a predictive model developed in [5] to express transmission coefficients on the back face of a hemicylindrical obstacle depending on RSDD. These data also allowed comparison of new data with Model S; the results obtained at small scale extended the validity of the model and larger-scale results also showed good agreement with the model. Obstacles with different diameters or shapes, various materials (deformable and non-deformable) would need to be studied in future to examine the validity range of the model. The difference in sensor behavior should also be investigated further.

Appendix

ISL trials' denomination

Distance charge –hemicylinder (M)	Trial reference
0.533	2304/2311/2316/2321
2	2410/2415/2438/2443
3.2	2448/2453/2458/2469/2516

IRSN trials' denomination

Distance charge –hemicylinder (M)	Trial reference
Free field	TIR1_CL_50g/ TIR2_CL_50g/ TIR3_CL_50g/ TIR4_CL_50g
0.27	TIR5_D27CYL_50g/ TIR6_D27CYL_50g/ TIR7_D27CYL_50g
1	TIR8_D100CYL_50g/ TIR9_D100CYL_50g/ TIR10_D100CYL_50g
1.6	TIR11_D160CYL_50g/ TIR12_D160CYL_50g/ TIR13_D160CYL_50g

Acknowledgements The authors thank profusely the technical staffs from PCE team (ISL) and ArianeGroup—Le Bouchet site for their work and help.

Open Access This article is licensed under a Creative Commons Attribution 4.0 International License, which permits use, sharing, adaptation, distribution and reproduction in any medium or format, as long as you give appropriate credit to the original author(s) and the source, provide a link to the Creative Commons licence, and indicate if changes were made. The images or other third party material in this article are included in the article's Creative Commons licence, unless indicated otherwise in a credit line to the material. If material is not included in the article's Creative Commons licence and your intended use is not permitted by statutory regulation or exceeds the permitted use, you will need to obtain permission directly from the copyright holder. To view a copy of this licence, visit <http://creativecommons.org/licenses/by/4.0/>.

References

- Zhi, X.-D., Qi, S.-B., Fan, F.: Temporal and spatial pressure distribution characteristics of hemispherical shell structure subjected to external explosion. *Thin Walled Struct.* **137**, 472–486 (2019). <https://doi.org/10.1016/j.tws.2019.01.021>
- Rigby, S.E., Tyas, A., Bennett, T., Fay, S.D., Clarke, S.D., Warren, J.A.: A numerical investigation of blast loading and clearing on small targets. *Int. J. Protect. Struct.* **5**, 253–274 (2014). <https://doi.org/10.1260/2041-4196.5.3.253>
- Tham, C.Y.: Numerical simulation on the interaction of blast waves with a series of aluminum cylinders at near-field. *Int. J. Impact*

- Eng. **36**, 122–131 (2009). <https://doi.org/10.1016/j.ijimpeng.2007.12.011>
- Kleine, H., Timofeev, E., Takayama, K.: Laboratory-scale blast wave phenomena—optical diagnostics and applications. *Shock Waves* **14**, 343–357 (2005). <https://doi.org/10.1007/s00193-005-0279-0>
- Trélat, S., Sturtzer, M.-O., Eckenfels, D.: Multi-scale experimental study of blast propagation around a hemi-cylindrical barrier. *WIT Trans. Built Environ.* **198**, 53–64 (2020). <https://doi.org/10.2495/SUSI200051>
- Kinney, G.F., Graham, K.J.: *Explosive Shocks in Air*. Springer, New York (1985). <https://doi.org/10.1007/978-3-642-86682-1>
- Cheval, K., Loiseau, O., Vala, V.: Laboratory scale tests for the assessment of solid explosive blast effects. Part I: free-field test campaign. *J. Loss Prev. Process Ind.* **23**, 613–621 (2010). <https://doi.org/10.1016/j.jlp.2010.05.001>
- Baker, W.E.: *Explosions in Air*. University of Texas Press, Austin (1973)
- Departement of Defense (USA) and United Facilities Criteria (UFC): *Structures to resist the effects of accidental explosions* (2008)
- Hopkinson, B.: *British Ordnance Board Minutes 13565*. The National Archives, Kew (1915)
- Allain, L.: *Barricade Influence on Blast Wave Propagation*. SNPE/Division Defense Espace, Vert-le-Petit (1994)
- Sha, S., Chen, Z., Jiang, X., Han, J.: Numerical investigations on blast wave attenuation by obstacles. *Proc. Eng.* **45**, 453–457 (2012). <https://doi.org/10.1016/j.proeng.2012.08.185>
- Sochet, I., Eveillard, S., Vinçont, J.Y., Piserchia, P.F., Rocourt, X.: Influence of the geometry of protective barriers on the propagation of shock waves. *Shock Waves* **27**, 209–219 (2017). <https://doi.org/10.1007/s00193-016-0625-4>
- Gautier, A., Sochet, I., Lapebie, E.: Analysis of 3D interaction of a blast wave with a finite wall. *Shock Waves* **32**, 273–282 (2022). <https://doi.org/10.1007/s00193-022-01081-7>
- Cheval, K., Loiseau, O., Vala, V.: Laboratory scale tests for the assessment of solid explosive blast effects. Part II: reflected blast series of tests. *J. Loss Prev. Process Ind.* **25**, 436–442 (2012). <https://doi.org/10.1016/j.jlp.2011.11.008>
- Ofengeim, D.K., Drikakis, D.: Simulation of blast wave propagation over a cylinder. *Shock Waves* **7**, 305–317 (1997). <https://doi.org/10.1007/s001930050085>
- Geva, M., Ram, O., Sadot, O.: The regular reflection/Mach reflection transition in unsteady flow over convex surfaces. *J. Fluid Mech.* **837**, 48–79 (2018). <https://doi.org/10.1017/jfm.2017.835>
- Glasstone, S., Dolan, P.J.: *The Effects of Nuclear Weapons*. United States Department of Defense, United States Department of Energy, London (1977)
- AMCP 706-181.: *Engineering Design Handbook: Explosion in Air, Part 1*. Army Material Command (1974)
- EBW Detonators.: *Teledyne Defense Electronics*. www.teledynedefenseelectronics.com/energetics/products/Pages/EBWDetonators.aspx. Accessed 25 Jan 2022
- Sturtzer, M.-O., Trélat, S., Sinniger, L.: Investigation on the post-processing of blast loading characteristics along a convex structure. *WIT Trans. Built Environ.* **198**, 41–52 (2020). <https://doi.org/10.2495/SUSI200041>
- Grosseuvres, R., Chaumeix, N., Bentaïb, A.: Pressure profiles measurements in ENACCEF facility for fast flame propagation. 17th International Topical Meeting on Nuclear Reactor Thermal Hydraulics (2017)

Publisher's Note Springer Nature remains neutral with regard to jurisdictional claims in published maps and institutional affiliations.